Advanced Characterization
https://www.sciltp.com/journals/ac

Review

Ultrathin Oxide Films for Heterogeneous Catalysis: Structure, Defects, and Reactivity

Shilpa Choyal [1], Soumyajit Rajak [1] and Nan Jiang [1,2,*]

[1] Department of Chemistry, University of Illinois Chicago, 845 West Taylor Street, Chicago, IL 60607, USA
[2] Department of Physics, University of Illinois Chicago, 845 West Taylor Street, Chicago, IL 60607, USA
* Correspondence: njiang@uic.edu

How To Cite: Choyal, S.; Rajak, S.; Jiang, N. Ultrathin Oxide Films for Heterogeneous Catalysis: Structure, Defects, and Reactivity. *Advanced Characterization* **2026**, *1*(1), 71–83. https://doi.org/10.53941/ac.2026.100006

Received: 9 May 2026
Revised: 5 June 2026
Accepted: 17 June 2026
Published: 22 June 2026

Abstract: Ultrathin oxide films on metal substrates have emerged as powerful model systems for heterogeneous catalysis, enabling direct correlation of atomic-scale structure with reactivity. Beyond serving as support for metal clusters, these films exhibit intrinsic catalytic activity, governed by film thickness, lattice mismatch, defect landscape, and the oxide-metal interfacial coupling, properties that often have no direct counterpart in bulk oxides. Separating these effects requires an atomistic characterization of structure, composition, and defect populations under increasingly realistic conditions. In this review, we survey the structural and electronic features of ultrathin oxide films, with particular emphasis on point defects, extended defects, and interfacial charge transfer, and connect each to representative catalytic behavior. Given the scope of this review, we limit our discussion to 3d transition metal oxides, wide band gap oxides, and charge transfer insulator type main group oxides. Finally, we outline the remaining experimental challenges and highlight emerging operando, time-resolved, and tip-enhanced techniques that deliver the spatial and chemical resolution needed to probe oxide surfaces under reaction-relevant conditions.

Keywords: catalysis; metal oxides; defects; ultrathin films; low-dimensional materials; scanning probe microscopy

1. Introduction

Oxide films play a central role in a wide range of modern technologies, from microelectronics and catalysis to energy conversion and storage. Well-ordered ultrathin oxide films grown on single-crystal metal supports have emerged as a model system for studying heterogeneous catalysis at the atomic scale using advanced surface-sensitive techniques such as scanning probe microscopy and spectroscopy [1]. In the context of model catalyst supports and metal/oxide interface, ultrathin oxide films consist of a few monolayers (typically 1–5 ML) of oxide grown on a single-crystal metal substrate and are generally no more than ~1 nm in thickness [2,3]. These films serve as well-defined templates for metal nanoparticles, allowing precise control over particle nucleation, size, and spatial distribution [3–5]. Fundamentally, however, they constitute a distinct class of materials in their own right. Their properties are governed not only by the oxide itself, but also by strong electronic and geometric coupling to the underlying metal substrate [6,7]. This metal-oxide coupling modifies the electronic structure, work function, and charge-transfer behavior of the system in ways that have no analog in bulk oxides and introduces film thickness as a continuously tunable parameter that can even shift the thermodynamic stability of the oxide phase relative to bulk [8]. When prepared under ultrahigh vacuum and controlled growth conditions, ultrathin oxide films thus offer a uniquely tractable platform for connecting geometric structure, electronic structure, and reaction kinetics.

A particularly important aspect of these films is the presence of structural features such as point defects, extended defects (including step edges and domain boundaries), and moiré superlattices arising from lattice mismatch with the substrate [9–13]. Such features introduce localized electronic states and modify adsorption energies, often acting as preferential nucleation sites for metal clusters and as active centers for catalytic reactions. Understanding how such defects form, evolve, and influence surface chemistry is therefore central to interpreting, and ultimately controlling, the reactivity of ultrathin oxide films.

Beyond their role as conventional catalyst supports, ultrathin oxide films on metal substrates can also adopt an inverse catalyst configuration, in which oxide nanoparticles or few-monolayer-thick films are deposited directly onto a metal surface, the structural mirror image of the conventional metal-on-oxide geometry [14]. This inverted architecture generates a high density of coordinatively unsaturated cation sites at the oxide-metal interface perimeter, which are stabilized by strong oxide-metal interactions and drive reactions that surpass those of conventional counterparts. In this review, we examine the structural and electronic features of ultrathin oxide films and link them to catalytic functions. Section 2 establishes how lattice mismatch, growth morphology, and substrate symmetry govern the structure of supported oxide films. Section 3 analyzes how point and extended defects govern catalytic behavior, illustrated through CO oxidation, water dissociation, and the oxygen evolution reaction. Section 4 discusses interfacial charge transfer and how it reshapes adsorbate states, cluster morphology, and reactivity. Section 5 closes with current challenges in atomic-scale defect characterization and an outlook on emerging operando, time-resolved, and tip-enhanced techniques that offer new opportunities to probe oxide surfaces under reaction-relevant conditions. In this review, we mainly discuss 3d transition metal, wide band gap oxides , and charge transfer insulator-type main group oxides. Owing to the breadth of oxide systems investigated in heterogeneous catalysis and the scope of the present review, a comprehensive discussion of all relevant oxide materials is beyond the scope of this article. Therefore, selected oxide systems that are not discussed in detail are summarized in Table 1, together with representative references for further reading.

Table 1. Additional relevant ultrathin oxide films grown on metal single-crystal supports.

Oxide	Substrate	Thickness	Structural Properties	Citation
SiO_2	Mo(112)	1 ML	2D network of corner-sharing [SiO_4] tetrahedra; one O per tetrahedron bonds to protruding Mo; chemically anchored.	[15]
SiO_2	Ru(0001)	Bilayer	Crystalline ↔ vitreous transition, Crystalline bilayer shows antiphase, rotational and domain boundaries; Stone-Wales-type defects.	[16]
TiO_2	Ag(100)	1 ML	Monolayer adopts a lepidocrocite-like TiO_2 structure, a 2D polymorph with no bulk counterpart.	[17]
MnO	Au(111)	1 ML	STM images resolve stripy and square defect patterns within MnO(100) islands; the stripy pattern is attributed to 1D vacancy rows; the square pattern is attributed to an ordered point vacancy superstructure on MnO(100) terraces.	[18]
MnO	Au(111)	1–2 ML	Atmosphere-driven phase transformation defects: monolayer-to-bilayer stacking faults at $Mn_3O_4 \rightarrow MnO(111)$ transition; domain boundaries between coexisting Mn_3O_4 and MnO(111) phases; interfacial disorder at MnO/Au(111) contact layer.	[19]
CoO and Co_3O_4	Pd(100)	1–2 ML	Multiple CoO_x phases are resolved at the atomistic level by STM, LEED, and XPS; phase boundaries between CoO and Co_3O_4 domains act as primary extended defects.	[20]
Cu_2O	Cu(111)	1–2 ML	Monolayer adopts honeycomb $Cu_2O(111)$-type structure; O vacancies and Cu_U vacancies are primary point defects; vacancy formation energy is strongly negative for Cu vacancies (DFT), making them the thermodynamically dominant defect species.	[21]
Cu_2O	Cu(100)	1 ML	Oxidation in O_2 at 80–260 °C yields missing-row reconstruction (MRR) at self-limiting 1 ML; annealing in UHV converts MRR to Cu(110)-facets coated with c(6×2) oxygen reconstruction; step-bunching and facet formation are the dominant structural defects.	[22]
Cu_2O	Au(111)	1–2 ML	Ordered Cu-vacancy superstructures within Cu_2O monolayer islands; vacancy ordering lowers surface energy and stabilizes the (111) polar termination.	[23]
Cu_2O	Au(111)	1–2 ML	Temperature-driven phase evolution: 1D oxide stripes at 450–550 K; planar (2 × 2) Cu_3O_2 honeycomb network at higher T; structurally well-defined domain boundaries between triangular, elongated, and stripe-like domains driven by strain minimization.	[24]

2. Structural Features of Ultrathin Oxide Films

The structural and electronic properties of ultrathin oxide films differ markedly from those of their bulk counterparts owing to reduced dimensionality and interfacial charge transfer between thin oxide film and substrate. Among the systems considered here, MgO films are the most closely related to their bulk analog. Their structural quality is primarily determined by the lattice mismatch with the underlying support, which introduces strain that is relieved through structural distortions within the oxide layer. MgO(100) films grown on Ag(100) and Mo(100) preserve the rock-salt structure of bulk MgO and display atomic geometries that closely resemble those of the bulk (100) surface. On Ag(100), with a lattice mismatch of only ~3%, the films are notably smooth and homogeneous [25,26]. Annealing followed by slow cooling can further enhance their structural quality [27,28]; in a systematic study spanning growth temperatures from 373 to 673 K, Bourguignon and co-workers reported the formation of larger MgO islands upon annealing at 573 K [29]. However, the MgO/Mo(100) film has a larger mismatch (~5%) that is accommodated by a network of dislocations in the oxide layer, and the resulting morphology depends strongly on film thickness [30].

Unlike MgO, many ultrathin oxide films adopt novel structures with no counterpart in the bulk. A classic example is alumina grown on NiAl(110) [12,31–33]. Scanning tunneling microscopy (STM) images reveal a network of bright lines attributed to grain boundaries between two reflection domains (A and B) and to anti-phase domain boundaries (A–A, B–B) within each domain. These line defects arise from the incommensurate registry between the alumina film and the NiAl(110) substrate [12,33] and serve as preferential nucleation sites for metal clusters at room temperature [11,34,35]. The system has been extensively studied as a support for catalyzed reactions such as the hydrogenation of unsaturated hydrocarbons [36–38], the dissociation of nitrous oxide [39,40], and the oxidation of carbon monoxide and methanol [41–43].

While metal oxides are frequently employed as support for metal nanoparticles, transition-metal ultrathin oxide films constitute an alternative class of well-defined model catalysts in their own right. Among these, vanadium oxides have been extensively investigated across a wide range of coverages and thicknesses [42,44–47]. Single-layer V_2O_5 adopts the same in-plane structure as a single sheet of bulk V_2O_5, which is itself a layered material in which V–O sheets stack via weak van der Waals interactions [48].

Another well-studied transition-metal oxide is FeO [13,49–54]. On noble metal surfaces, FeO forms ordered ultrathin films with moiré superstructures driven by lattice mismatch. On Pt(111), the FeO bilayer has a surface lattice constant of 3.09 Å and forms a long-range moiré superstructure with a period of 26.4 Å [50,53]. Annealing a Pt-supported $Fe_3O_4(111)$ film to 800 K in vacuum yields a single FeO(111) layer; although bulk wüstite (FeO) is itself rock-salt, the supported single layer instead adopts a hexagonal bilayer geometry stabilized by the Pt(111) substrate [52]. This underscores the crucial role of the substrate in stabilizing oxide phases that are inaccessible in the bulk. Extending these studies to gold, our group has demonstrated that FeO undergoes substrate symmetry-driven structural evolution on both Au(111) and Au(100) [13,54]. On Au(100), FeO forms coexisting embedded and stepped islands with a twofold-symmetric moiré pattern, in contrast to the hexagonal moiré observed on Au(111) (Figure 1). Despite these morphological differences, FeO retains its chemical identity, as confirmed by a characteristic Raman mode at 985 cm^{-1} (Figure 1b,d) measured by tip-enhanced Raman spectroscopy (TERS) [54]. The moiré superlattices partition the films into spatially inequivalent regions and create distinct adsorption environments that are expected to modulate surface reactivity and catalytic behavior, as discussed in later sections.

Beyond morphology, the polarity and orientation of ultrathin oxide films can also differ markedly from those of their bulk counterparts. A representative example is provided by NiO, in which the polar NiO(111) surface termination, which is unstable in the bulk owing to its uncompensated electrostatic dipole, can be stabilized in ultrathin film form [55]. On Au(111), NiO preferentially grows in the nonpolar (100) orientation at room temperature, but annealing to ~573 K yields a well-ordered NiO(111) monolayer with a $p(2 \times 2)$ reconstruction. This reconstruction is consistent with the theoretically predicted octopolar stabilization mechanism [55,56]. A similar temperature-dependent structural evolution is observed for NiO on Ag(100), where the thermodynamically favored (1×1) phase replaces the metastable (2×1) structure upon heating. In this system, strain is relaxed through the incorporation of bilayer NiO patches, which constitute ~30% of the coverage. At these bilayer rims, the first NiO layer in direct contact with Ag becomes partially metallized through hybridization with the substrate, while the second layer retains a more insulating, bulk-like character with a reduced density of states (DOS) near the Fermi level [57,58]. Ultrathin TiO_x films on metal substrates likewise display structural diversity that is absent in bulk TiO_2. These films nucleate as small islands with multiple coexisting orientations and reduced stoichiometries, reflecting the combined influence of substrate symmetry and the oxygen chemical potential during growth [59–62]. Taken together, these examples illustrate how substrate–oxide interactions can stabilize structural motifs that have no direct counterpart in the corresponding bulk oxides, including polar terminations, surface reconstructions, and reduced polymorphs. The electronic consequences of this structural diversity, and the role of defects in governing catalytic reactions, are discussed in the following section.

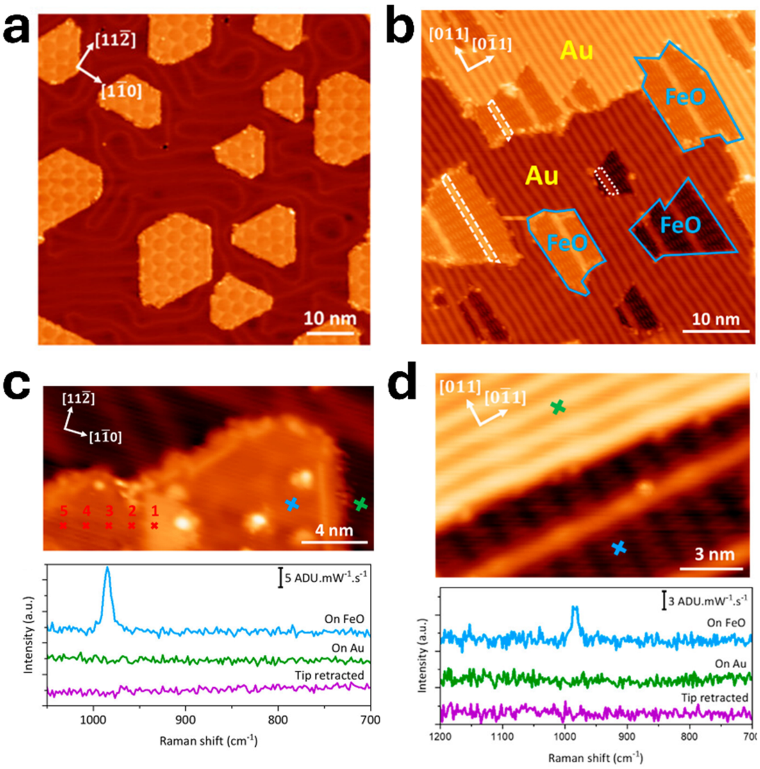

Figure 1. STM and TERS characterization of FeO/Au(111). (**a**) STM topography of FeO/Au(111) displaying a hexagonal moiré superlattice. (**b**) STM image of FeO/Au(100), where FeO nanoislands are highlighted by blue polygons, and the wrinkled surface region with the white strips. (**c**,**d**) Corresponding TERS spectra acquired from FeO/Au(111) surface and FeO/Au(100), respectively, collected from the regions shown in the STM images above. Reprinted with permission from [54] (CCBY4.0).

3. Defect Engineering and Catalytic Activity in Ultrathin Oxide Films

3.1. Point Defects

Point defects play a crucial role in the catalytic activity of ultrathin oxide films. Among them, oxygen vacancies, commonly referred to as color centers, have been studied most extensively. These vacancies act as electron-trapping centers and mediate surface electron transfer by donating charge from the oxide to adsorbates. They also serve as preferential sites for the nucleation of metal atoms and clusters through strong local metal-oxide interactions [63,64]. The density and chemical nature of oxygen vacancies vary significantly among oxides. Reducible oxides, such as TiO_2, typically exhibit relatively high surface-vacancy concentrations [65], while non-reducible oxides such as MgO support far fewer such vacancies [66,67].

To systematically investigate defect-mediated reactivity, oxygen vacancies in ultrathin oxide films can be introduced in a controlled manner through treatments such as electron bombardment. As-grown MgO/Ag(100) films possess very few intrinsic defects, providing a clean baseline for such measurements. By combining low-temperature STM and scanning tunneling spectroscopy (STS) with ultrahigh vacuum electron paramagnetic resonance (UHV-EPR), individual color centers have been unambiguously identified and characterized on these films. As shown in Figure 2a, paramagnetic F^+ vacancies form preferentially at island edges and corners rather than on terraces, in agreement with the lower defect formation energies predicted for low-coordinated sites [68]. Complementary STS measurements further identified diamagnetic neutral F centers through their distinctive in-gap electronic states; the assignments are corroborated by density functional theory (DFT) calculations. Notably, the charge state of individual vacancies can be tuned via interaction with the STM tip, establishing low-coordinated oxygen vacancies in ultrathin MgO films as electronically distinct and catalytically relevant surface defects [66,67].

Point defects exert a strong influence on metal nucleation and catalytic behavior. STM studies of Au deposited on MgO/Mo(100) demonstrate that Au atoms nucleate preferentially at defect sites, which act as strong anchoring points for cluster formation [69]. This defect-dominated nucleation mechanism is further supported by embedded-cluster calculations, which show that metal nucleation on MgO is governed by surface F (anionic vacancy) and V (hole) centers rather than by regular terrace sites. These findings illustrate how the charge state and electron affinity of a vacancy directly control both metal–oxide bond strength and resultant charge on metal adatoms, which can range from neutral to M^+ or to lattice-incorporated cations such as Pd^{2+} and Ag^{2+} at Mg-vacancy sites [70]. As a result, defect-free MgO surfaces are essentially inert, whereas defect-rich MgO films exhibit significantly higher and more complex reactivity. Theoretical work further suggests that oxygen vacancies can directly participate in reaction pathways rather than acting solely as passive anchoring sites [9,71]. The electronic consequences of point defects can be directly probed using vibrational spectroscopy of probe molecules such as CO. On regular, non-defective MgO films, CO adsorbed on metallic Au clusters exhibits a stretching frequency near 2120 cm^{-1}; after the creation of oxygen vacancies and subsequent Au deposition, the stretching frequency shifts to 2070 cm^{-1} [72]. This red shift for clusters on defect-rich films indicates that Au atoms bound to oxygen vacancies acquire a negative charge ($Au^{\delta-}$), in agreement with DFT calculations [73].

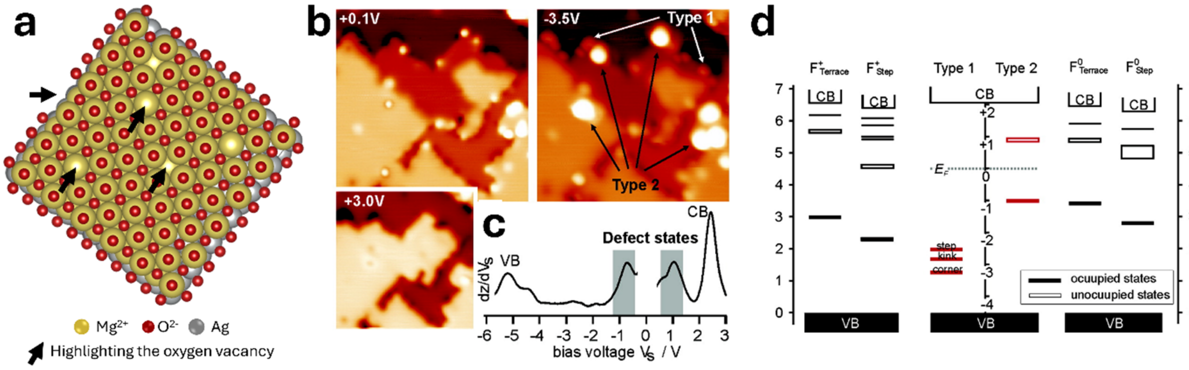

Figure 2. (**a**) Schematic illustration of oxygen vacancy defects in MgO/Ag(100). (**b**) STM images at different bias voltages showing the distribution of charged defects on the surface of MgO(001) thin films. (**c**) dz/dV_S spectrum acquired at an F^0 center (type 2 defects). (**d**) Calculated energy levels of F^+, F^0 centers located at terrace and step sites, including a summary of energy levels associated with type 1 (F^+) and type 2 (F^0) defects. (**b**–**d**) Reprinted with permission from [66]. Copyright 2006, American Chemical Society.

F centers in MgO can exist in three charge states, denoted F^0, F^+, and F^{2+}, according to whether they contain two, one, or zero trapped electrons, respectively. These defects introduce impurity levels in the MgO band gap; for terrace centers, the F^0 level lies near mid-gap while the F^+ level lies above it, closer to the conduction-band edge (Figure 2) [66]. On ultrathin MgO films supported on metal, the underlying substrate can stabilize different charge states via spontaneous charge transfer, depending on the position of the F^0/F^+ levels relative to the metal Fermi level. For MgO/Mo(100), where the effective work function is ~2 eV, only F^0 centers are stable, and any F^+ centers would immediately be filled by tunneling from the metal. In contrast, for MgO/Ag(100) with $\phi \approx 3$ eV, the F^0 level is pinned near E_F, and F^+ centers are thermodynamically favored [74]. The stability of a given charge state also depends on defect location (surface vs. interface) and film thickness, both of which modify the level positions and the dielectric screening. Beyond the tip-induced switching demonstrated above [54,55], the systematic control of vacancy charge states under operating catalytic conditions remains an open challenge, but the framework above offers a promising route to tailor the electronic and catalytic properties of oxide surfaces through controlled defect charging.

Oxygen vacancies also play a critical role in catalytic cycles such as the Mars–van Krevelen mechanism, in which the oxide lattice itself supplies oxygen to reactants. A prominent example is CO oxidation on monolayer FeO films supported on Pt(111). Under reactive O_2-rich conditions, the FeO(111) bilayer transforms into an oxygen-rich O-Fe-O trilayer in which an additional oxygen layer sits on top of the Fe sub-lattice [51,75,76]. This trilayer provides lattice oxygen that oxidizes CO to CO_2, leaving behind an oxygen vacancy that is subsequently replenished by gas-phase oxygen [75]. Notably, this high catalytic reactivity diminishes in thicker FeO films, underscoring that the ultrathin geometry of the oxide is essential to its catalytic function. A similar mechanism operates for single-layered ZnO/Au(111), where interfacially intercalated oxygen activates lattice oxygen adjacent to the intercalated species, enabling Mars-van Krevelen-type CO oxidation [77].

In ceria-based oxide, oxidation also proceeds via the Mars-van Krevelen mechanism. Surface and subsurface oxygen vacancies can be resolved by STM, with the electrons left behind upon oxygen removal localizing on neighboring Ce ions to form Ce^{3+} species. These reduced centers tend to aggregate into vacancy dimers and linear clusters that preferentially expose Ce^{3+} sites highly relevant to redox chemistry [78,79]. Similarly, ultrathin $CeO_2(111)$ films grown on Pt(111) exhibit a rich defect landscape, including surface and subsurface vacancies, vacancy trimers, extended vacancy arrays, and hydroxylated species, closely resembling the defect chemistry of bulk ceria. The morphology and defect density of ceria films depend strongly on preparation conditions. For instance, reactive deposition on Au(111) produces well-ordered $CeO_2(111)$ nanoislands with oxygen vacancies, making CeO_2/Au(111) a model inverse oxide catalyst [80]. Similarly, CeO_x nanoparticles on Cu(111) promote O_2 dissociation and drive the formation of Cu_2O_{1+x} surface oxides at the interface. During CO/O_2 cycles, these systems exhibit reversible Ce^{4+}/Ce^{3+} redox behavior and enable oxygen spillover, leading to catalytic activities comparable to or exceeding noble metals [81].

3.2. Extended Defects

Beyond point defects, ultrathin oxide films frequently contain more complex linear features, including step edges and domain boundaries. These line defects introduce distinct electronic states that significantly modify surface chemistry. The under-coordinated species at step edges and kink sites often exhibit enhanced reactivity, enabling dissociation reactions that do not proceed on flat terraces. For instance, CO oxidation on partially covered FeO/Pt(111) initiates preferentially at island edges [82,83]. The active sites at this perimeter have been identified as coordinatively unsaturated ferrous (Fe^{2+}) cations, which activate molecular oxygen, while CO adsorbs on adjacent Pt sites; this spatial separation of the two reactants prevents the CO self-poisoning that limits CO oxidation on bulk Pt. After CO_2 formation and desorption, the edge Fe site is regenerated, making the FeO-Pt perimeter a robust and self-sustaining redox interface.

For ZnO/Ag(111) films, structural and electronic inhomogeneities such as moiré patterns and Ag clusters modulate the local density of states (LDOS) of the ZnO conduction band, and TERS combined with STS has revealed that this modulation controls local heating efficiency and electron-phonon coupling strength. Positions of elevated conduction band LDOS correspond to higher vibrational temperatures, and the ratio of the TERS-derived temperature map to the spatially filtered STS map yields a relative electron-enhanced coupling map at ~2 nm resolution, with coupling locally enhanced at atomic-scale defect sites [84]. The sensitivity of these properties to structural disorder becomes increasingly pronounced with film thickness. High-resolution imaging has shown that 3 ML ZnO films develop dislocation defects with local lattice displacement of ~0.8 Å and distorted honeycomb structures that are absent in the more ordered 2 ML films (Figure 3a,b). This structural degradation with increasing thickness was attributed to a partial transition from the planar h-BN-like geometry of the thinner film toward a corrugated wurtzite-like surface structure, highlighting how film thickness fundamentally shapes the defect landscape of supported oxides [85].

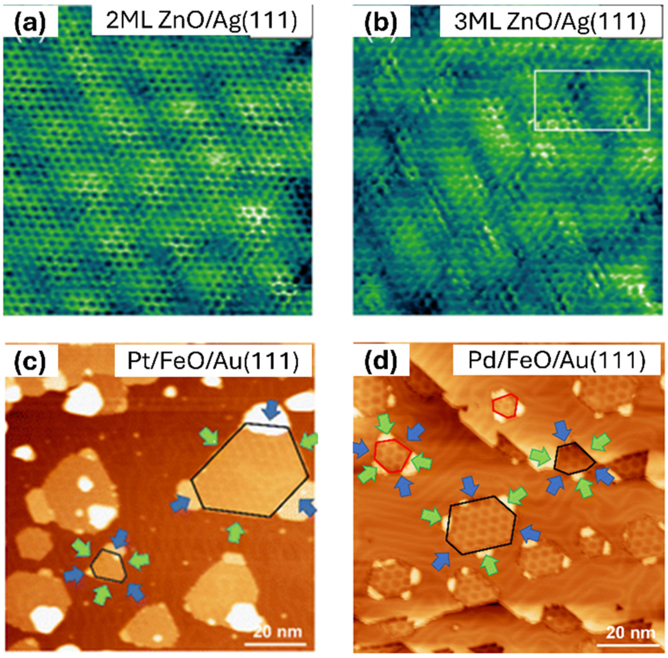

Figure 3. STM topography of ZnO and FeO ultrathin films. (**a**,**b**) STHM images (10 nm × 10 nm) of 2 ML and 3 ML ZnO films on Ag(111), respectively. Reprinted with permission from [85]. Copyright 2018 American Physical Society. (**c**,**d**) STM images (100 nm × 100 nm) of FeO/Au(111) illustrate selective growth of Pt and Pd on FeO/Au(111), with Pt preferentially blocking O-terminated edge sites and Pd preferentially blocking Fe-terminated edge sites. Reprinted with permission from [13]. Copyright 2022 Royal Society of Chemistry.

Similar structure–reactivity relationships have been identified for NiO films supported on Au(111). In this system, edge and NiO_x-Ni interfacial sites form highly active Lewis acid-base pairs that dominate water dissociation, while flat oxide terraces and defect-poor regions remain largely inert [86]. Furthermore, in the electrocatalytic oxygen evolution reaction (OER), two-dimensional NiO films on Au(111) outperform thicker, three-dimensional NiO islands, further emphasizing the importance of maximizing edge density [87]. These observations demonstrate that designing films with smaller islands and a higher density of edge sites can directly enhance catalytic activity.

Beyond their role as active sites, extended defects can also direct the spatial organization of metal adatoms for catalysis. Al_2O_3 films grown on NiAl(110) exhibit multiple extended defect types, including step edges, reflection domain boundaries, and anti-phase boundaries. STM studies have shown that Pd atoms nucleate exclusively along these defect lines, forming ordered one-dimensional arrays [35]. Similarly, a study of the FeO/Au(111) moiré structure demonstrated that Pt preferentially decorates oxygen-terminated edges, whereas Pd targets Fe-terminated edges (Figure 3c,d), both of which are critical sites for CO oxidation [13]. This edge-selective metal decoration provides a pathway to control active-ensemble formation and tune catalytic selectivity. Taken together, these examples establish extended defects as both reactive sites in their own right and as templates that direct the assembly of catalytically active metal ensembles. Beyond such intrinsic structural features, the properties of ultrathin oxide films can be further tailored through interfacial charge transfer, as discussed below.

4. Charge Transfer in Ultrathin Oxide Films

Ultrathin oxide films on metal substrates exhibit charge-transfer phenomena that are significantly weaker or absent in bulk oxides. When an insulating film only a few monolayers thick is supported on a metal, the effective work function of the metal–oxide stack, together with the oxide band structure, sets the alignment between the metal Fermi level and the frontier orbitals of an adsorbate, and thereby controls whether electrons can tunnel through the film into adsorbed atoms, clusters, or molecules, or flow in the opposite direction. At such small thicknesses, strong interfacial coupling and reduced dimensionality produce electronic states and responses that do not occur in extended oxide crystals [88]. Even perfectly ordered, defect-free ultrathin films can support significant electron tunneling between the metal and species bound on the oxide surface, enabling direct charge exchange across the film and stabilizing adsorbate charge states that would be inaccessible on bulk oxides [6]. MgO provides a prototypical example. DFT calculations comparing Pd and Au atom adsorption on bulk-like MgO(001) and MgO/Mo(100) show that Pd atoms remain essentially neutral in both cases, whereas Au becomes anionic (Au^-) on the MgO/Mo(100) film but not on the bulk-like MgO surface [6]. On thick MgO, the unoccupied part of the Au 6s level lies in the MgO band gap and above the metal Fermi level; when the oxide is thinned, and the metal-oxide work function is lowered by 1–2 eV, this electron-affinity level is pulled below the Fermi level, making electron tunneling from the metal energetically favorable [89]. The extra electron localizes at the Au-MgO interface and induces a polaronic distortion of the MgO lattice (outward relaxation of the underlying Mg and inward relaxation of the surrounding O), which stabilizes the charged adsorbate [90].

Low-temperature STM combined with DFT on MgO/Ag(100) provides direct experimental evidence of charge transfer in ultrathin films [91]. On a 3 ML MgO film, Au adatoms self-organize into a long-range ordered lattice with a well-defined nearest-neighbor distance, indicating strong repulsive interactions between like-charged species (Figure 4). In STM, Au adatoms appear as “sombrero-shaped” protrusions, a contrast that can be reproduced in DFT-based simulations only for negatively charged Au. In contrast, Pd adatoms on the same film, and Au atoms on bare Ag(001) (Figure 4) or on thick MgO, remain randomly distributed and show neutral-like STM contrast. This is consistent with DFT predictions that Pd’s low electron affinity prevents charging, and that through-film charge transfer is effective only for thin oxide spacers and high-electron-affinity metals [6,91].

Another consequence of charge transfer is its effect on metal nanoparticle morphology and stabilization. Charged particles often experience a stronger attraction to the substrate, resulting in different equilibrium shapes than their neutral counterparts [92,93]. For instance, DFT calculations have shown that a Au_{20} cluster, which is tetrahedral (3D) in vacuum, becomes planar (2D) in its equilibrium shape when adsorbed on a 2 ML MgO/Mo film [92]. On bulk MgO, the 3D cluster is more stable than the 2D form by ~1.2 eV, but on the ultrathin film, a flat island is favored by ~3.3 eV. This reversal arises from charge localization at the Au-MgO interface upon electron transfer from the Mo substrate, which increases the Au–oxide adhesion by ~1 eV per Au atom and drives the cluster to spread out for maximum interfacial contact [92]. This prediction has been confirmed experimentally by comparing Au growth on 3 ML and 8 ML MgO films on Ag(100) [93]. On 3 ML MgO, Au nucleates on both Mg and O sites and, after annealing, forms monolayer-high 2D islands, whereas on the 8 ML film, it preferentially occupies O sites and develops into 3D clusters resembling those of Au on bulk MgO(001) [93]. Together with charge-state measurements on single Au adatoms, these results establish that the degree of charge transfer at the metal-oxide interface controls not only the electronic structure but also the shape and wetting behavior of Au islands on ultrathin oxide films, providing a route to tune cluster morphology for catalysis.

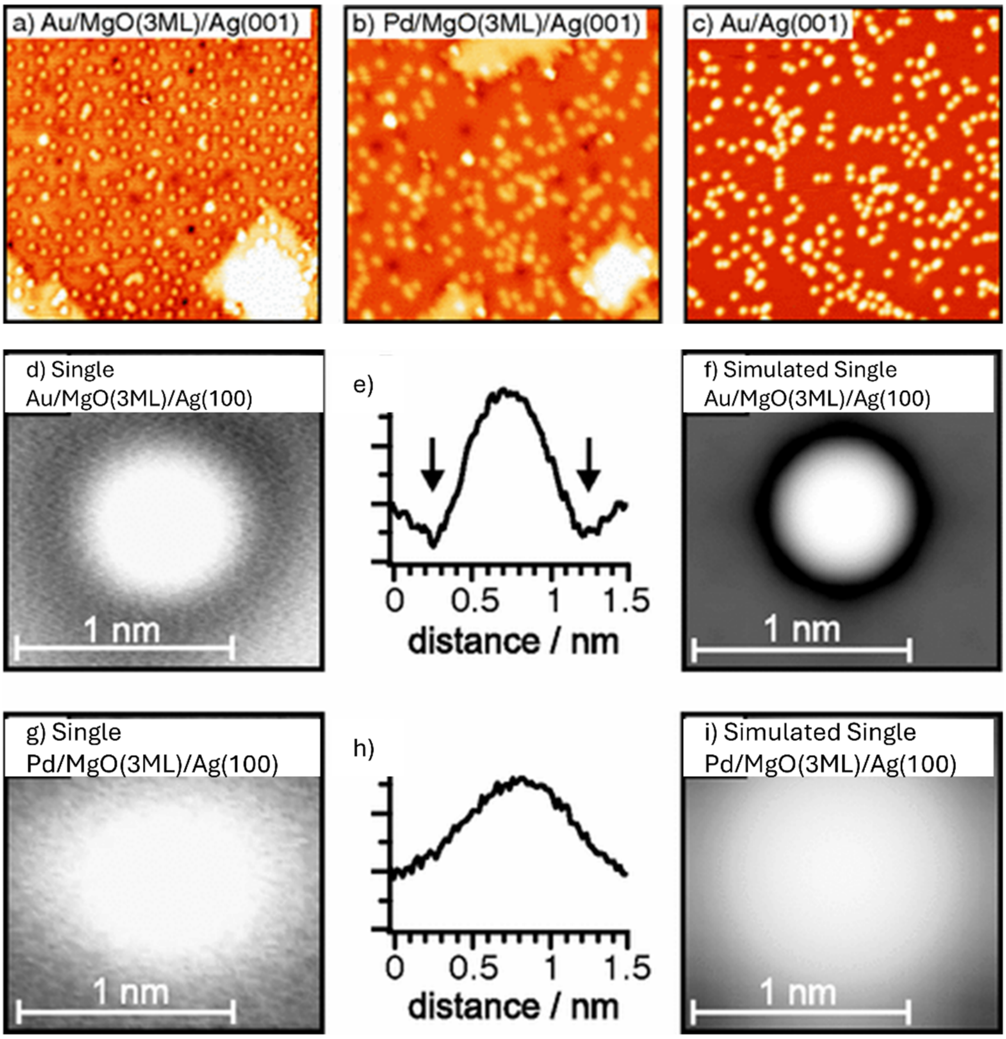

Figure 4. STM images (30 nm × 30 nm) of (**a**) Au atoms adsorbed on 3 ML MgO films. (**b**) Pd atoms adsorbed on 3 ML MgO films, and (**c**) Au atom adsorbed on bare Ag(001). (**d**–**f**) Experimental STM images and height profiles, and corresponding simulated STM images of single Au, and (**g**–**i**) Pd atoms on the surface of 3 ML MgO/Ag(001). Reprinted with permission from [88]. Copyright 2007 American Physical Society.

Charge transfer through oxide films is equally important for molecules with high electron affinity. DFT calculations predict that O_2 adsorbed on ultrathin MgO/Ag(100) films forms a superoxo-like O_2^- species, stabilized by electron transfer from the metal and polaronic distortion of the MgO lattice [94]. This prediction has been experimentally verified by low-temperature EPR on O_2 dosed onto a 4 ML MgO/Mo(001) film. The spectra exhibit an axial g-tensor ($g_{zz} \approx 2.072$) characteristic of O_2^-; the signal intensity decays with increasing film thickness and vanishes around 15 ML, in full agreement with the proposed electron-tunneling model [6,7]. The g-tensor components differ from those of O_2^- on bulk MgO powders, indicating stronger polaronic relaxation in the ultrathin oxide films. An analogous activation has been reported for NO_2 on MgO, where a metal support converts weakly bound, nearly neutral NO_2 on MgO into a strongly bound nitrite anion (NO_2^-) through charge transfer from the substrate, which simultaneously strengthens the oxide-metal interface [95]. Collectively, these examples underscore the generality of adsorbate charging mediated by electron tunneling through ultrathin oxide films.

5. Outlook and Challenges

Ultrathin metal-oxide films are evolving from idealized surface-science model systems into a versatile platform for probing and engineering catalytic phenomena at the atomic scale. Their properties, arising from reduced dimensionality and tunable defect landscapes, enable catalytic behaviors that are fundamentally distinct from those of bulk oxides. The next generation of model systems, including multicomponent ultrathin films, doped oxides, and dynamically evolving interfaces, introduces heterogeneity across multiple length scales and will demand corresponding advances in characterization. A central priority is the development of correlative and multimodal characterization frameworks that integrate complementary probes within a unified experimental environment. Combining scanning probe microscopy with chemically sensitive techniques (tip-enhanced Raman spectroscopy [42], X-ray photoelectron spectroscopy, and synchrotron-based methods [96]) offers a direct route to linking atomic structure, local composition, and reactivity at individual sites. Such approaches are particularly critical for ultrathin oxide films, where catalytic activity is often governed by highly localized features such as defects, step edges, and interfacial charge-transfer regions, which are the features emphasized throughout this review.

A second priority is bridging the gap between the static, ultra-high-vacuum measurements that dominate the literature and the dynamic, reaction-relevant conditions under which catalysis actually occurs. Active sites at metal-oxide interfaces are often transient and stabilized only under reaction conditions, motivating the integration of operando and time-resolved capabilities into the experimental toolkit [97–100]. Combining ultrafast spectroscopy with operando setups would, in principle, give access to charge-carrier dynamics, lattice dynamics, transient intermediates, and structural restructuring on the timescales over which they actually occur, although preserving sensitivity and minimizing probe-induced perturbations remains significantly challenging. Techniques such as terahertz (THz) pump–probe spectroscopy, transient absorption spectroscopy, and time-resolved X-ray scattering provide access to elementary steps across femtosecond-to-second timescales. For ultrathin oxide films, these approaches are most relevant for elucidating charge-transfer dynamics [101,102], polaron formation [103], and electron–phonon interactions [104] at metal–oxide interfaces, processes that are central to catalytic function but remain poorly understood at the relevant timescales. Combining such temporal resolution with the sub-nanometer spatial sensitivity of scanning probe techniques would enable spatiotemporally resolved characterization of catalytic systems [105–107].

The future of ultrathin metal-oxide films in heterogeneous catalysis will be defined by the ability to observe, quantify, and ultimately control catalytic processes at the level of individual active sites and elementary steps. As such it will depend on the continued evolution of sub-nanoscale, vibronic, and time-resolved characterization techniques. Beyond serving as idealized model systems, ultrathin metal-oxide films are poised to become testbeds for next-generation characterization strategies, where methodological innovation directly informs catalyst design. The convergence of spatial, temporal, and chemical resolution achieved through integrated, operando, and data-driven approaches will be key to unlocking a truly predictive understanding of catalytic functions at the atomic scale.

Author Contributions

S.C.: conceptualization, writing-original draft; S.R.: writing-original draft; N.J.: conceptualization, supervision, reviewing and editing. All authors have read and agreed to the published version of the manuscript.

Funding

N.J., S.C. and S.R. gratefully acknowledge financial support from the National Science Foundation (NSF) DMR-2211474.

Institutional Review Board Statement

Not applicable.

Informed Consent Statement

Not applicable.

Data Availability Statement

Not applicable

Conflicts of Interest

The authors declare no conflict of interest.

Use of AI and AI-Assisted Technologies

During the Preparation of this work, the authors used ChatGPT to improve language. After using this tool, the authors reviewed and edited the content as needed and take full responsibility for the content of the published article.

References

1. Nilius, N. Properties of Oxide Thin Films and Their Adsorption Behavior Studied by Scanning Tunneling Microscopy and Conductance Spectroscopy. *Surf. Sci. Rep.* **2009**, *64*, 595–659.
2. Freund, H.J.; Pacchioni, G. Oxide Ultra-Thin Films on Metals: New Materials for the Design of Supported Metal Catalysts. *Chem. Soc. Rev.* **2008**, *37*, 2224–2242.
3. Giordano, L.; Pacchioni, G. Oxide Films at the Nanoscale: New Structures, New Functions, and New Materials. *Acc. Chem. Res.* **2011**, *44*, 1244–1252.
4. Henry, C.R. Surface Studies of Supported Model Catalysts. *Surf. Sci. Rep.* **1998**, *31*, 231–325.
5. Freund, H.J. Model Studies in Heterogeneous Catalysis. *Chem. Eur. J.* **2010**, *16*, 9384–9397.
6. Pacchioni, G.; Giordano, L.; Baistrocchi, M. Charging of Metal Atoms on Ultrathin MgO/Mo(100) Films. *Phys. Rev. Lett.* **2005**, *94*, 226104.
7. Frondelius, P.; Hellman, A.; Honkala, K.; et al. Charging of Atoms, Clusters, and Molecules on Metal-Supported Oxides: A General and Long-Ranged Phenomenon. *Phys. Rev. B* **2008**, *78*, 085426.
8. Campbell, C.T. Transition Metal Oxides: Extra Thermodynamic Stability as Thin Films. *Phys. Rev. Lett.* **2006**, *96*, 066106.
9. König, T.; Simon, G.H.; Heinke, L.; et al. Defects in Oxide Surfaces Studied by Atomic Force and Scanning Tunneling Microscopy. *Beilstein J. Nanotechnol.* **2011**, *2*, 1–14.
10. Luo, Y.; Wu, Y. Defect Engineering of Nanomaterials for Catalysis. *Nanomaterials* **2023**, *13*, 1116.
11. Schmid, M.; Shishkin, M.; Kresse, G.; et al. Oxygen-Deficient Line Defects in an Ultrathin Aluminum Oxide Film. *Phys. Rev. Lett.* **2006**, *97*, 046101.
12. Libuda, J.; Winkelmann, F.; Bäumer, M.; et al. Structure and Defects of an Ordered Alumina Film on NiAl(110). *Surf. Sci.* **1994**, *318*, 61–73.
13. Liu, D.; Li, L.; Gedara, B.S.A.; et al. The Selective Blocking of Potentially Catalytically Active Sites on Surface-Supported Iron Oxide Catalysts. *Mater. Chem. Front.* **2023**, *7*, 476–482.
14. Senanayake, S.D.; Stacchiola, D.; Rodriguez, J.A. Unique Properties of Ceria Nanoparticles Supported on Metals: Novel Inverse Ceria/Copper Catalysts for CO Oxidation and the Water-Gas Shift Reaction. *Acc. Chem. Res.* **2013**, *46*, 1702–1711.
15. Weissenrieder, J.; Kaya, S.; Lu, J.L.; et al. Atomic Structure of a Thin Silica Film on a Mo(112) Substrate: A Two-Dimensional Network of SiO_4 Tetrahedra. *Phys. Rev. Lett.* **2005**, *95*, 076103.
16. Klemm, H.W.; Prieto, M.J.; Xiong, F.; et al. A Silica Bilayer Supported on Ru(0001): Following the Crystalline-to Vitreous Transformation in Real Time with Spectro-Microscopy. *Angew. Chem. Int. Ed.* **2020**, *59*, 10587–10593.
17. Atrei, A.; Ferrari, A.M.; Szieberth, D.; et al. Lepidocrocite-like Structure of the TiO_2 Monolayer Grown on Ag(100). *Phys. Chem. Chem. Phys.* **2010**, *12*, 11587–11595.
18. Chen, P.; Zhu, Y.; Ge, T.; et al. Scanning Tunneling Microscopy of MnO_x Ultrathin Films on Au(111). *Surf. Sci.* **2023**, *730*, 122248.
19. Liu, Y.; Zhang, R.; Ling, Y.; et al. Dynamic Structural Evolution of Mn-Au Alloy and MnO_x Nanostructures on Au(111) under Different Atmospheres. *J. Phys. Chem. C* **2021**, *125*, 15335–15342.
20. Schmidt, M.C.; Smyczek, J.; Hubert, P.; et al. Growth of Ultrathin Cobalt Oxide Films on Pd(100): Refined Structural Model. *Surf. Sci.* **2024**, *742*, 122451.
21. Zhang, R.; Li, L.; Frazer, L.; et al. Atomistic Determination of the Surface Structure of Cu_2O(111): Experiment and Theory. *Phys. Chem. Chem. Phys.* **2018**, *20*, 27456–27463.
22. Shields, S.S.; Gupta, J.A. STM Study of Surface Restructuring of Oxidized Cu(100). *Surf. Sci.* **2024**, *740*, 122403.
23. Zhu, B.; Huang, W.; Lin, H.; et al. Vacancy Ordering in Ultrathin Copper Oxide Films on Cu(111). *J. Am. Chem. Soc.* **2024**, *146*, 15887–15896.
24. Möller, C.; Fedderwitz, H.; Noguera, C.; et al. Temperature-Dependent Phase Evolution of Copper-Oxide Thin-Films on Au(111). *Phys. Chem. Chem. Phys.* **2018**, *20*, 5636–5643.
25. Schintke, S.; Messerli, S.; Pivetta, M.; et al. Insulator at the Ultrathin Limit: MgO on Ag(001). *Phys. Rev. Lett.* **2001**, *87*, 276801.
26. Freund, H.J.; Heyde, M.; Kuhlenbeck, H.; et al. Chapter Model Systems in Heterogeneous Catalysis at the Atomic Level: A Personal View. *Sci. China Chem.* **2020**, *63*, 426–447.
27. Pal, J.; Smerieri, M.; Celasco, E.; et al. Morphology of Monolayer MgO Films on Ag(100): Switching from Corrugated Islands to Extended Flat Terraces. *Phys. Rev. Lett.* **2014**, *112*, 126102.
28. Pal, J.; Smerieri, M.; Celasco, E.; et al. How Growing Conditions and Interfacial Oxygen Affect the Final Morphology of MgO/Ag(100) Films. *J. Phys. Chem. C* **2014**, *118*, 26091–26102.
29. Ouvrard, A.; Niebauer, J.; Ghalgaoui, A.; et al. Characterization of Thin MgO Films on Ag(001) by Low-Energy Electron Diffraction and Scanning Tunneling Microscopy. *J. Phys. Chem. C* **2011**, *115*, 8034–8041.
30. Benedetti, S.; Benia, H.M.; Nilius, N.; et al. Morphology and Optical Properties of MgO Thin Films on Mo(001). *Chem. Phys. Lett.* **2006**, *430*, 330–335.

31. Jaeger, R.M.; Kuhlenbeck, H.; Freund, H.J.; et al. Formation of a Well-Ordered Aluminium Oxide Overlayer by Oxidation of NiAl(110). *Surf. Sci.* **1991**, *259*, 235–252.
32. Kresse, G.; Schmid, M.; Napetschnig, E.; et al. Structure of the Ultrathin Aluminum Oxide Film on NiAl(110). *Science* **2005**, *308*, 1440–1442.
33. Kulawik, M.; Nilius, N.; Rust, H.P.; et al. Atomic Structure of Antiphase Domain Boundaries of a Thin Al_2O_3 Films on NiAl(110). *Phys. Rev. Lett.* **2003**, *91*, 256101.
34. Bäumer, M.; Libuda, J.; Sandell, A.; et al. The Growth and Properties of Pd and Pt on Al_2O_3/NiAl(110). *Ber. Bunsenges. Phys. Chem.* **1995**, *99*, 1381–1386.
35. Hansen, K.H.; Worren, T.; Stempel, S.; et al. Palladium Nanocrystals on Al_2O_3: Structure and Adhesion Energy. *Phys. Rev. Lett.* **1999**, *83*, 4120–4123.
36. Brandt, B.; Fischer, J.H.; Ludwig, W.; et al. Isomerization and Hydrogenation of Cis-2-Butene on Pd Model Catalyst. *J. Phys. Chem. C* **2008**, *112*, 11408–11420.
37. Doyle, A.M.; Shaikhutdinov, S.K.; Freund, H.J. Surface-Bonded Precursor Determines Particle Size Effects for Alkene Hydrogenation on Palladium. *Angew. Chem. Int. Ed.* **2005**, *44*, 629–631.
38. Doyle, A.M.; Shaikhutdinov, S.K.; Freund, H.J. Alkene Chemistry on the Palladium Surface: Nanoparticles vs Single Crystals. *J. Catal.* **2004**, *223*, 444–453.
39. Schauermann, S.; Johánek, V.; Laurin, M.; et al. Low Temperature Decomposition of NO on Ordered Alumina Films. *Chem. Phys. Lett.* **2003**, *381*, 298–305.
40. Johánek, V.; Schauermann, S.; Laurin, M.; et al. Site Occupation and Activity of Catalyst Nanoparticles Monitored by in Situ Vibrational Spectroscopy. *Angew. Chem. Int. Ed.* **2003**, *42*, 3035–3038.
41. Libuda, J.; Freund, H.J. Molecular Beam Experiments on Model Catalysts. *Surf. Sci. Rep.* **2005**, *57*, 157–298.
42. Sock, M.; Surnev, S.; Ramsey, M.G.; et al. Adsorption and Reaction of CO on Vanadium Oxide-Pd(111) "Inverse" Model Catalysts: An HREELS Study. *Top. Catal.* **2000**, *14*, 15–23.
43. Schauermann, S.; Hoffmann, J.; Johánek, V.; et al. Catalytic Activity and Poisoning of Specific Sites on Supported Metal Nanoparticles. *Angew. Chem. Int. Ed.* **2002**, *41*, 2532–2535.
44. Lewis, K.B.; Oyama, S.T.; Somorjai, G.A. The Preparation and Reactivity of Thin, Ordered Films of Vanadium Oxide on Au(111). *Surf. Sci.* **1990**, *233*, 75–83.
45. Leisenberger, F.P.; Surnev, S.; Vitali, L.; et al. Nature, Growth, and Stability of Vanadium Oxides on Pd(111). *J. Vac. Sci. Technol. A* **1999**, *17*, 1743–1749.
46. Surnev, S.; Kresse, G.; Ramsey, M.G.; et al. Novel Interface-Mediated Metastable Oxide Phases: Vanadium Oxides on Pd(111). *Phys. Rev. Lett.* **2001**, *87*, 086102.
47. Schoiswohl, J.; Sock, M.; Surnev, S.; et al. V_2O_3(0001) Surface Terminations: From Oxygen- to Vanadium-Rich. *Surf. Sci.* **2004**, *555*, 101–117.
48. Blum, R.P.; Niehus, H.; Hucho, C.; et al. Surface Metal-Insulator Transition on a Vanadium Pentoxide (001) Single Crystal. *Phys. Rev. Lett.* **2007**, *99*, 226103.
49. Shaikhutdinov, S.; Ritter, M.; Weiss, W. Hexagonal Heterolayers on a Square Lattice: A Combined STM and LEED Study of FeO (111) on Pt (100). *Phys. Rev. B* **2000**, *62*, 7535–7541.
50. Ritter, M.; Ranke, W.; Weiss, W. Growth and Structure of Ultrathin FeO Films on Pt(111) Studied by STM and LEED. *Phys. Rev. B* **1998**, *57*, 7240.
51. Sun, Y.N.; Qin, Z.H.; Lewandowski, M.; et al. Monolayer Iron Oxide Film on Platinum Promotes Low Temperature CO Oxidation. *J. Catal.* **2009**, *266*, 359–368.
52. Weiss, W.; Ranke, W. Surface Chemistry and Catalysis on Well-Defined Epitaxial Iron-Oxide Layers. *Prog. Surf. Sci.* **2002**, *70*, 1–151.
53. Galloway, H.C.; Benítez, J.J.; Salmeron, M. The Structure of Monolayer Films of FeO on Pt(111). *Surf. Sci.* **1993**, *298*, 127–133.
54. Liu, D.; Li, L.; Jiang, N. Nanoscale Chemical Probing of Metal-Supported Ultrathin Ferrous Oxide via Tip-Enhanced Raman Spectroscopy and Scanning Tunneling Microscopy. *Chem. Biomed. Imaging* **2024**, *2*, 345–351.
55. Hannemann, H.; Ventrice, C.A.; Bertrams, T.; et al. Scanning Tunneling Microscopy on the Growth of Ordered NiO Layers on Au(111). *Phys. Status Solidi A* **1994**, *146*, 289–297.
56. Ventrice, C.A.; Bertrams, T.; Hannemann, H.; et al. Stable Reconstruction of the Polar (111) Surface of NiO on Au(111). *Phys. Rev. B* **1994**, *49*, 5773.
57. Steurer, W.; Allegretti, F.; Surnev, S.; et al. Metamorphosis of Ultrathin Ni Oxide Nanostructures on Ag(100). *Phys. Rev. B* **2011**, *84*, 115446.
58. Steurer, W.; Surnev, S.; Fortunelli, A.; et al. Scanning Tunneling Microscopy Imaging of NiO(100)(1 × 1) Islands Embedded in Ag(100). *Surf. Sci.* **2012**, *606*, 803–807.

59. Wu, Q.H.; Fortunelli, A.; Granozzi, G. Preparation, Characterisation and Structure of Ti and Al Ultrathin Oxide Films on Metals. *Int. Rev. Phys. Chem.* **2009**, *28*, 517–576.
60. Dulub, O.; Hebenstreit, W.; Diebold, U. Imaging Cluster Surfaces with Atomic Resolution: The Strong Metal-Support Interaction State of Pt Supported on TiO_2(110). *Phys. Rev. Lett.* **2000**, *84*, 3646.
61. Bowker, M.; Stone, P.; Morrall, P.; et al. Model Catalyst Studies of the Strong Metal–Support Interaction: Surface Structure Identified by STM on Pd Nanoparticles on TiO_2(110). *J. Catal.* **2005**, *234*, 172–181.
62. Barcaro, G.; Agnoli, S.; Sedona, F.; et al. Structure of Reduced Ultrathin TiO_x Polar Films on Pt(111). *J. Phys. Chem. C* **2009**, *113*, 5721–5729.
63. Haas, G.; Menck, A.; Brune, H.; et al. Nucleation and Growth of Supported Clusters at Defect Sites: Pd/MgO (001). *Phys. Rev. B* **2000**, *61*, 11105–11108.
64. Frank, M.; Bäumer, M.; Kühnemuth, R.; et al. Metal Atoms and Particles on Oxide Supports: Probing Structure and Charge by Infrared Spectroscopy. *J. Phys. Chem. B* **2001**, *105*, 8569–8576.
65. Diebold, U. The Surface Science of Titanium Dioxide. *Surf. Sci. Rep.* **2003**, *48*, 53–229.
66. Sterrer, M.; Heyde, M.; Novicki, M.; et al. Identification of Color Centers on MgO(001) Thin Films with Scanning Tunneling Microscopy. *J. Phys. Chem. B* **2006**, *110*, 46–49.
67. Sterrer, M.; Fischbach, E.; Risse, T.; et al. Geometric Characterization of a Singly Charged Oxygen Vacancy on a Single-Crystalline MgO(001) Film by Electron Paramagnetic Resonance Spectroscopy. *Phys. Rev. Lett.* **2005**, *94*, 186101.
68. Pacchioni, G.; Pescarmona, P. Structure and Stability of Oxygen Vacancies on Sub-Surface, Terraces, and Low-Coordinated Surface Sites of MgO: An Ab Initio Study. *Surf. Sci.* **1998**, *412*, 657–671.
69. Benia, H.M.; Lin, X.; Gao, H.J.; et al. Nucleation and Growth of Gold on MgO Thin Films: A Combined STM and Luminescence Study. *J. Phys. Chem. C* **2007**, *111*, 10528–10533.
70. Ferrari, A.M.; Pacchioni, G. Metal Deposition on Oxide Surfaces: A Quantum-Chemical Study of the Interaction of Rb, Pd, and Ag Atoms with the Surface Vacancies of MgO. *J. Phys. Chem.* **1996**, *100*, 9032–9037.
71. Ferrari, A.M.; Pacchioni, G. Electronic Structure of F and V Centers on the MgO Surface. *J. Phys. Chem.* **1995**, *99*, 17010–17018.
72. Sterrer, M.; Yulikov, M.; Fischbach, E.; et al. Interaction of Gold Clusters with Color Centers on MgO(001) Films. *Angew. Chem. Int. Ed.* **2006**, *45*, 2630–2632.
73. Del Vitto, A.; Giordano, L.; Pacchioni, G.; et al. CO Adsorption on Ni_4 and Ni_8 Clusters Deposited on Regular and Defect Sites of the MgO(001) Surface. *Surf. Sci.* **2005**, *575*, 103–114.
74. Giordano, L.; Martinez, U.; Pacchioni, G.; et al. F and F^+ Centers on MgO/Ag(100) or MgO/Mo(100) Ultrathin Films: Are They Stable? J. *Phys. Chem. C* **2008**, *112*, 3857–3865.
75. Sun, Y.; Giordano, L.; Goniakowski, J.; et al. The Interplay between Structure and CO Oxidation Catalysis on Metal-Supported Ultrathin Oxide Films. *Angew. Chem. Int. Ed.* **2010**, *49*, 4418–4421.
76. Giordano, L.; Lewandowski, M.; Groot, I.M.N.; et al. Oxygen-Induced Transformations of an FeO(111) Film on Pt(111): A Combined DFT and STM Study. *J. Phys. Chem. C* **2010**, *114*, 21504–21509.
77. Liu, C.; Lin, L.; Wu, H.; et al. Activating Lattice Oxygen of Single-Layer ZnO for the Catalytic Oxidation Reaction. *Phys. Chem. Chem. Phys.* **2023**, *25*, 20121–20127.
78. Grinter, D.C.; Ithnin, R.; Pang, C.L.; et al. Defect Structure of Ultrathin Ceria Films on Pt(111): Atomic Views from Scanning Tunnelling Microscopy. *J. Phys. Chem. C* **2010**, *114*, 17036–17041.
79. Esch, F.; Fabris, S.; Zhou, L.; et al. Electron Localization Determines Defect Formation on Ceria Substrates. *Science* **2005**, *309*, 752–755.
80. Ma, S.; Rodriguez, J.; Hrbek, J. STM Study of the Growth of Cerium Oxide Nanoparticles on Au(111). *Surf. Sci.* **2008**, *602*, 3272–3278.
81. Yang, F.; Graciani, J.; Evans, J.; et al. CO Oxidation on Inverse CeO_x/Cu(111) Catalysts: High Catalytic Activity and Ceria-Promoted Dissociation of O_2. *J. Am. Chem. Soc.* **2011**, *133*, 3444–3451.
82. Fu, Q.; Li, W.X.; Yao, Y.; et al. Interface-Confined Ferrous Centers for Catalytic Oxidation. *Science* **2010**, *328*, 1141–1144.
83. Zhang, K.; Li, L.; Shaikhutdinov, S.; et al. Carbon Monoxide Oxidation on Metal-Supported Monolayer Oxide Films: Establishing Which Interface Is Active. *Angew. Chem. Int. Ed.* **2018**, *130*, 1275–1279.
84. Liu, S.; Wolf, M.; Kumagai, T. Nanoscale Heating of an Ultrathin Oxide Film Studied by Tip-Enhanced Raman Spectroscopy. *Phys. Rev. Lett.* **2022**, *128*, 206803.
85. Liu, S.; Shiotari, A.; Baugh, D.; et al. Enhanced Resolution Imaging of Ultrathin ZnO Layers on Ag(111) by Multiple Hydrogen Molecules in a Scanning Tunneling Microscope Junction. *Phys. Rev. B* **2018**, *97*, 195417.
86. Zhao, S.; Lin, L.; Huang, W.; et al. Design of Lewis Pairs via Interface Engineering of Oxide−Metal Composite Catalyst for Water Activation. *J. Phys. Chem. Lett.* **2021**, *12*, 1443–1452.

87. Zhang, H.; Zhang, H.; Wang, R.; et al. Enhancing Oxygen Evolution Reaction with Two-Dimensional Nickel Oxide on Au (111). *Catalysts* **2024**, *14*, 284.
88. Freysoldt, C.; Rinke, P.; Scheffler, M. Ultrathin Oxides: Bulk-Oxide-Like Model Surfaces or Unique Films? *Phys. Rev. Lett.* **2007**, *99*, 086101.
89. Giordano, L.; Cinquini, F.; Pacchioni, G. Tuning the Surface Metal Work Function by Deposition of Ultrathin Oxide Films: Density Functional Calculations. *Phys. Rev. B* **2006**, *73*, 045414.
90. Giordano, L.; Martinez, U.; Sicolo, S.; et al. Observable Consequences of Formation of Au Anions from Deposition of Au Atoms on Ultrathin Oxide Films. *J. Chem. Phys.* **2007**, *127*, 144713.
91. Sterrer, M.; Risse, T.; Martinez Pozzoni, U.; et al. Control of the Charge State of Metal Atoms on Thin MgO Films. *Phys. Rev. Lett.* **2007**, *98*, 096107.
92. Ricci, D.; Bongiorno, A.; Pacchioni, G.; et al. Bonding Trends and Dimensionality Crossover of Gold Nanoclusters on Metal-Supported MgO Thin Films. *Phys. Rev. Lett.* **2006**, *97*, 036106.
93. Sterrer, M.; Risse, T.; Heyde, M.; et al. Crossover from Three-Dimensional to Two-Dimensional Geometries of Au Nanostructures on Thin MgO(001) Films: A Confirmation of Theoretical Predictions. *Phys. Rev. Lett.* **2007**, *98*, 206103.
94. Hellman, A.; Klacar, S.; Grönbeck, H. Low Temperature CO Oxidation over Supported Ultrathin MgO Films. *J. Am. Chem. Soc.* **2009**, *131*, 16636–16637.
95. Grönbeck, H. Mechanism for NO_2 Charging on Metal Supported MgO. *J. Phys. Chem. B* **2006**, *110*, 11977–11981.
96. Ajayi, T.M.; Shirato, N.; Rojas, T.; et al. Characterization of Just One Atom Using Synchrotron X-rays. *Nature* **2023**, *618*, 69–73.
97. Kim, Y.; So, Y.; Kim, M.; et al. Comprehensive Review of In-Situ and Operando Measurements in Oxide Materials. *Curr. Appl. Phys.* **2026**, *89*, 87–94.
98. Peng, M.; Li, C.; Wang, Z.; et al. Interfacial Catalysis at Atomic Level. *Chem. Rev.* **2025**, *125*, 2371–2439.
99. Thapa, S.; Paudel, R.; Blanchet, M.D.; et al. Probing Surfaces and Interfaces in Complex Oxide Films via in Situ X-ray Photoelectron Spectroscopy. *J. Mater. Res.* **2021**, *36*, 26–51.
100. Yang, C.; Wöll, C. IR Spectroscopy Applied to Metal Oxide Surfaces: Adsorbate Vibrations and Beyond. *Adv. Phys. X* **2017**, *2*, 373–408.
101. Butler, K.T.; Dringoli, B.J.; Zhou, L.; et al. Ultrafast Carrier Dynamics in $BiVO_4$ Thin Film Photoanode Material: Interplay between Free Carriers, Trapped Carriers and Low-Frequency Lattice Vibrations. *J. Mater. Chem. A.* **2016**, *4*, 18516–18523.
102. Köper, M.; Hempel, H.; Harbauer, K.; et al. Grain Boundaries Limit the Charge Carrier Transport in Pulsed Laser Deposited α-$SnWO_4$ Thin Film Photoabsorbers. *ACS Appl. Energy Mater.* **2020**, *3*, 4320–4330.
103. Ziwritsch, M.; Müller, S.; Hempel, H.; et al. Direct Time-Resolved Observation of Carrier Trapping and Polaron Conductivity in $BiVO_4$. *ACS Energy Lett.* **2016**, *1*, 888–894.
104. Chen, P.; Xu, X.; Koenigsmann, C.; et al. Size-Dependent Infrared Phonon Modes and Ferroelectric Phase Transition in $BiFeO_3$ Nanoparticles. *Nano Lett.* **2010**, *10*, 4526–4532.
105. Luo, Y.; Martin-Jimenez, A.; Pisarra, M.; et al. Imaging and Controlling Coherent Phonon Wave Packets in Single Graphene Nanoribbons. *Nat. Commun.* **2023**, *14*, 3484.
106. Luo, Y.; Sheng, S.; Schirato, A.; et al. Visualizing Hot Carrier Dynamics by Nonlinear Optical Spectroscopy at the Atomic Length Scale. *Nat. Commun.* **2025**, *16*, 4999.
107. Kimura, K.; Tamaki, R.; Lee, M.; et al. Ultrafast On-Demand Exciton Formation in a Single-Molecule Junction by Tailored Terahertz Pulses. *Science* **2025**, *387*, 1077–1082.